X-ray Chemical Imaging of Mn-doped Co/TiO_2 Pellets reveals the significance of Cobalt Carbide Formation and Distribution on CO conversion and Alcohol Selectivity during Fischer Tropsch Synthesis

Andrew Beale

andrew.beale@ucl.ac.uk

University College London https://orcid.org/0000-0002-0923-1433

Danial Farooq

University College London

Matthew Potter

University College London

Sebastian Stockenhuber

University College London

Jay Pritchard

University College London

Antonis Vamvakeros

Imperial College London https://orcid.org/0000-0002-4745-0602

Stephen Price

Finden ltd

Jakub Drnec

ESRF https://orcid.org/0000-0002-9520-1555

Ben Ruchte

IXRF Systems

James Paterson

BP (United Kingdom) https://orcid.org/0000-0003-1016-5776

Mark Peacock

bp, Applied Sciences, Innovation & Engineering

Article

Keywords:

Posted Date: February 27th, 2024

DOI: https://doi.org/10.21203/rs.3.rs-3961226/v1

Additional Declarations: Yes there is potential Competing Interest. Andrew M. Beale is an equal shareholder and Chief Scientific Officer of Finden Ltd.

Abstract

X-ray diffraction/scattering computed tomography (XRS-CT) were used to create 2D images, with 20 μm resolution, of passivated Co/TiO_2/Mn Fischer Tropsch catalyst extrudates post-reaction after 300 h on stream under industrially relevant conditions. This combination of scattering techniques provided unprecedented insights into both the spatial variation of the various cobalt phases and the influence of increasing Mn loading has on this. Also observed is the presence of a wax coating throughout the extrudate and its capacity to preserve the Co/Mn species in the same state as in the reactor. Correlating these findings with catalytic performance, highlights the crucial phases and active sites within Fischer Tropsch catalysts required for understanding the tunability of the product distribution between saturated hydrocarbons or oxygenate and olefin products. In particular a Mn loading of 3 wt. % led to an optimum equilibrium between the amount of hexagonal close-packed Co and Co_2C phases resulting in maximum oxygenate selectivity. XRS-CT revealed Co_2C to be located on the extrudates' periphery, while metallic Co phases were more prevalent towards the centre, possibly due to a lower [CO] ratio there. Reduction at 450°C of a 10 wt. % Mn sample resulted in $MnTiO_3$ formation which inhibited carbide formation and alcohol selectivity. It is suggested that small MnO particles promote Co carburisation by decreasing the CO dissociation barrier and the Co_2C phase promotes CO non-dissociative adsorption leading to increased oxygenate selectivity. This study highlights the influence of Mn on catalyst structure and function and the importance of studying catalysts under industrially relevant reaction times.

Introduction

The transition to a sustainable future relies on the widespread adoption of circular economy principles such as utilising waste and maximising resource efficiency which are essential in our quest to achieve net-zero emissions by 2050. Various X to liquid (XTL) technologies have been studied to explore the feasibility of converting alternative carbon sources such as biomass and waste/oil residues to valuable hydrocarbon products [1]. The Fischer Tropsch (FT) process, involving the conversion of syngas (mixture of CO and H_2) into liquid hydrocarbons, is an established process from the mid-1920s [2]. The process can play a vital role in mitigating the effects of climate change by providing a pathway to carbon-neutral fuels when using renewable hydrogen [3]. However, it has recently emerged that the selectivity of the process can be tuned to also produce high-value chemical products (olefins and alcohols) from industrial waste streams and captured carbon dioxide (CO_2) converted to CO [4,5].

Cobalt, iron, nickel and ruthenium are the most recognised catalytically active elements in the FT process although ruthenium is too expensive for commercial application [6]. Sasol developed Fischer-Tropsch (FT) processes in Sasolburg (Sasol I-III) utilising Fe catalysts from 1955 until the 1990s [7]. Recently, cobalt catalysts have been favoured industrially due to their low-methane selectivity and CO_2 tolerance [8]. In 1993, Shell adopted cobalt catalysts in a commercial-scale plant in Malaysia [9]. Shell further advanced its capabilities by establishing the world's largest Gas-to-Liquids (GTL) plant in Qatar in 2010, known as the

Shell GTL Pearl plant, with a capability of producing 140,000 barrels of liquid products per day [9]. Additionally, BP and Johnson Matthey developed FT technology which was successfully deployed in 2002 in a 300 bbl/day demonstration plant in Nikisiki, Alaska [8]. Furthermore, Fulcrum BioEnergy are a licensee of BP-Johnson Matthey CANS™ catalyst carriers technology [10] for its Sierra BioFuels plant in Nevada which aims to convert approximately 175,000 million tonnes of municipal solid waste into 42 million litres of renewable FT product per year. The FT CANS™ technology has also been licensed to Strategic Biofuels for the Louisiana Green Fuels project (LGF) which aims to convert 1 million tonnes of forestry waste feedstock into 120 million litres of renewable diesel per year [11].

Both the face-centred cubic (FCC) and the hexagonal close-packed (HCP) Co metal phases are known to be active in the FT process. The HCP phase has demonstrated higher activity [12–17] whilst it is found that the HCP phase transforms more readily into cobalt carbide (Co_2C) where they share a similar stacking sequence (ABAB) [18]. Whilst the Co_2C phase was previously thought to be inactive [19], recent research has found it to play a vital role in increased alcohol selectivity [20,21]. Co_2C is found to be stable at FT conditions and is formed inversely proportionally to the H_2/CO ratio and FT reaction temperature [22]. Co_2C nanoprisms demonstrated higher selectivity towards lower olefins which was attributed to exposed (101) and (020) facets [23] while the active site for higher olefins requires further research. Zhao et al. investigated model catalytic systems particularly focusing on the complementarity between metallic cobalt and Co_2C phases, including Co on the surface of Co_2C nanoparticles and Co_2C on the surface of Co nanoparticles and found that both exhibited similar alcohol selectivity indicating that the Co-Co_2C interface present in both systems was the probable active site [24]. However, Co on the Co_2C led to higher olefin selectivity which was attributed to the lower H_2/CO syngas ratio. Alkyl chain formation involves both CO dissociation and hydrogenation whilst alcohol formation involves associative CO adsorption into the alkyl chain which is proposed to occur on the Co-Co_2C interface [23,25,26].

A broad range of noble metal promoters have been found to improve FT catalytic performance [27] and in particular there has been recent interest in the role of Mn promoters in improving selectivity to high value oxygenates such as long-chain alcohols (C_8 – C_{20+}) [28]. Mn-promoted FT Co catalysts have demonstrated higher activity, improved selectivity to C_{5+} hydrocarbons and olefins and lower methane production due to the inhibition of hydrogenation activity and a decrease in the CO dissociation barrier [28,29]. In particular, Mn promotes disproportionation and dissociation of CO leading to carburisation of Co to Co_2C. The CO bond dissociation is suggested by Johnson et al. to be promoted by Lewis acid-base interactions between Mn^{2+} ions, situated on the edges of MnO clusters which cover Co particles, and the O atoms of adsorbed CO [30]. This is similar to the La dopant on activated carbon which also promotes Co_2C formation due to the presence of small La oxide clusters in close proximity to Co particles [31]. The thermodynamic stability of the Co_2C phase is improved due to a reduction in Co particle size and increased surface area. Zhu et al. reported that CO dissociation occurs at O vacancies in MnO_X leading to surface C and carbonate formation [32]. It is suggested that Mn inhibits H_2 uptake on the metallic Co

surface further contributing to a lower H_2/CO ratio promoting Co_2C formation [24]. Carbon atoms are thought to diffuse into Co vacancy defects to form the Co_2C [24]. Mn promotion was also found to improve cobalt dispersion and reduce the Co particle size [28,33].

TiO_2 is found to be a suitable catalyst support material with high surface area, chemical stability and a strong metal support interaction [34]. Titania supports exhibit a low surface area and high porosity and pore size, enabling improved dispersion of the active Co metal phase [35].

Due to the multiple complex interactions between different catalytic phases and promoters present it is important to characterise the chemical and physical environments of FT catalyst under industrial conditions to gain a true insight into their performance. Industrial catalysts are often pelletised into millimetre-sized bodies in order to reduce pressure-drop in the reactor [36]. The larger size of these extrudates, compared to powders, leads to spatial variation which require techniques with spatial resolution to comprehend their structure and identify genuine active sites [37]. Recent advances in X-ray diffraction- and Pair distribution function- computed tomography techniques (XRD-CT and PDF-CT) allow the examination of both crystalline and amorphous phases present in catalytic body with spatial resolution to gain a better understanding of catalyst structure and function relationships under industrial relevant conditions [38–40]. Additionally, X-ray fluorescence (XRF) element mapping can be used to provide valuable information about the distribution and concentration of different elements within the catalyst extrudate [41]. This is crucial for understanding how the catalyst composition changes before and after the reaction.

This study investigates the role of Mn promotion in Co/TiO_2 Fischer Tropsch catalysts in increasing alcohol and olefin selectivity using XRD-CT and PDF-CT techniques, performed on recovered catalyst after 300 h of reaction under FT conditions. Conducting these experiments post-reaction enabled the exploration of active phases present at more industrially relevant reaction times that usually cannot be reached during typically time-limited *in situ* beamtime experiments.

Methods

Catalytic Reaction

10 wt. % Co/TiO_2 extruded trilobe pellets with varied Mn loadings (0, 1, 2, 3, 5 and 10 wt. %) were produced by dissolving cobalt nitrate hexahydrate and manganese acetate tetrahydrate in water, along with P25 titania powder. The Co and Mn solution was impregnated onto the titania, thoroughly mixed, and then extruded to form extrudates with a diameter of 1.6 mm in trilobe shape. The extrudates were dried at 120°C for 24 h and calcined at 300°C in a box furnace. Subsequently, the reduction process was conducted at 300°C in 100% H_2 at atmospheric pressure for 25 h before introducing syngas. The catalysts had a fixed 10 wt. % loading of Co and increasing Mn loading corresponded with decreasing TiO_2 content. An additional 10% Mn sample was activated at 450°C. 1 g of each catalyst was run under

FT conditions for 300 h in 2:1 H_2:CO syngas with a GHSV of 3000 h^{-1} at 30 barg and 210–240°C, where higher Mn catalyst required higher temperatures to match conversion. Online GC analysis was used to measure standard metrics such as conversion, short chain selectivity, and productivity as performed in a previous study [42]. Conversion and selectivity were assessed by comparing the argon internal standard to the input and output of CO using online gas chromatographs. Online measurements covered C_1 to C_{20}, and selectivity was calculated based on the internal standard. The selectivity for C_5 and higher hydrocarbons (C_{5+}) was determined as 100 minus the sum of C_1-C_4 products. The reactor was an 8-channel high throughput unit, with common gas feeds and pressures but individual liner temperature control. The catalysts were loaded into each liner ahead of leak testing, activation and FT synthesis. The extrudates were unloaded from the reactor without removing their wax coating (generated *in situ* from the production of long-chain hydrocarbons) as a self-passivating procedure, using only a short nitrogen purge step. A 5% Mn sample was also reacted for 150 h in FT conditions and recovered for analysis, using an analogous 4-channel reactor [43].

XRD-CT and PDF-CT measurements

The pellets were mounted in glass capillaries (3 mm diameter and 0.1 mm wall thickness) and secured with quartz wool. The μ-XRD-CT and μ-PDF-CT scans of the extrudates were performed at ESRF, ID31. A picture of the experimental setup is presented in Figure S1. A monochromatic pencil X-ray beam at 91 keV with a size 5 x 22 μm was used with a 50 ms acquisition time and a PILATUS CdTe 2M detector. A motorised stage was used to perform the tomographic scans with 120 translation steps (20 μm step size) over 180 ° (1.5 ° step size) utilising an interlaced approach [44]. The detector was moved from 0.370 m to 1.87 m to collect both PDF and XRD data, respectively, for each cross-section of each sample. The XRD images were calibrated using a CeO_2 standard reference, which was also used to model instrumental broadening of the diffraction patterns.

Tomographic Reconstruction

After calibration of every 2D diffraction image, pyFAI software [45] and python scripts were used to azimuthally integrate the images to a 1D powder diffraction pattern [46]. Air scattering was removed and the sinograms were centred using MATLAB scripts [47]. The filtered back projection algorithm was used to reconstruct the XRD-CT data. The data was processed into a three-dimensional array (249 x 249 x 924) where the 249 x 249 pixels corresponded to the 2D cross-section image size and the 924 points stored the complete diffraction pattern for each pixel. The resultant spatial resolution of each pixel was approximately 20 μm.

XRD Refinements

TOPAS Academic v7 was used to perform Rietveld analysis on the XRD-CT data for quantitative phase analysis and structure determination [48]. The diffraction pattern of a CeO_2 calibrant was used to calculate the instrument parameters for the TOPAS refinements (peak shape, primary radius and slit radius). The

full profile Rietveld analysis was initially performed on the summed diffraction pattern of the entire XRD-CT data to arrive at a suitable starting model for subsequent sequential refinement of the data in each pixel. Scale factors were refined for each phase followed by lattice parameters and then crystallite size parameters. Crystallographic information of the phases refined are available in Table S1. Firstly, the known dominant TiO_2 polymorphs, rutile and anatase, in the catalyst phase were included and refined in the input file. Next, cobalt metal phases (FCC and HCP) and cobalt carbide were refined. Due to the similar X-ray scattering effects coefficients of Mn and Co, their oxides could not be refined separately. It is known that mixed metal oxide spinels form (Salazar-Contreras et al., 2019) which could be detected by an expansion in the lattice parameter of the cobalt oxide phases (CoO and Co_3O_4) in the refinement since Mn ions are larger than Co ions.

The trilobe cross-sections were divided into individual one-pixel thick layers from the outer periphery to the centre using a MATLAB script. The script searched the immediately surrounding pixels of each pixel for non-zero values (pixels without diffraction data) to create a mask of the outermost layer of the extrudate. This layer was then subtracted, and a mask was created for the next subsequent layer. This process was repeated until all layers were characterised with a mask. These individual layers were summed, and the corresponding diffraction patterns were analysed with the Rietveld method using TOPAS to investigate the chemical structure as a function of the distance from the pellet centre. 2D spatial maps of the refined parameters were produced.

Generating the PDF and Real-space Refinements

The atomic pair distribution function (PDF) was produced by Fourier transforming the XRD-CT data using PDFGetX3 software (Juhas et al., 2013) which also performed various additive and multiplicative corrections, for instance due to finite Q range and atomic scattering factors. The PDFs were calculated to a Q_{max} of 25.3 $Å^{-1}$ and to a r value of 50 Å with a $Q_{maxinst}$ parameter of 25.3 $Å^{-1}$. Initially, the mean XRD pattern was transformed into a mean PDF pattern and analysed to build a good starting model for the subsequent sequential refinement that would be performed. Real-space Rietveld refinement was performed using TOPAS (Coelho, 2018) which minimises a residual between the experimental PDF and a calculated PDF using a least-squares optimisation approach. Various macros were used to implement PDF real-space refinement on TOPAS [49,50]. Firstly, peak broadening and dampening due to instrument factors were refined using the CeO_2 standard which were subsequently fixed for the refinement of the PDF of the sample. Scale, crystallite size, lattice parameters and atomic displacement parameters (B_{eq}) were refined sequentially for the mean pattern. There is a gradual dissipation of correlated motion as a function of *r* and this was included in the refinement by modelling the atomic displacement parameters using a spherical function [50]. Screening of additional structures that were potentially present in the sample was carried out using a web-based programme, 'PDF in the Cloud' (Yang et al., 2020). The programme enabled automated structure refinements to be carried out, using CIF files sourced from a crystallographic server. The refinements were carried out on difference PDFs that were obtained from the difference between the experimental data and the known refined support phases, anatase and rutile, and cobalt phases to determine if any unexpected phases were present. Like in the XRD processing, separate

layers from the extrudate trilobes were transformed into PDF's and refined to further study the extrudate structure as a function of distance from the centre of the pellets. The refined parameters were then processed in to 2D phase spatial maps using MATLAB.

Non-Negative Matrix Factorisation (NMF)

Due to the large amount of XRD patterns (~ 10,000s) present in an XRD-CT dataset, automated analysis is required. However, this can lead to diffuse components and phases being missed. Non-Negative Matrix Factorization (NMF) can be used to computationally extract the individual components or phases present in a dataset [51]. NMF was used in this study to ensure the comprehensive identification of all components within the data, preventing the omission of diffuse components and phases that could occur with manual analysis. The Python scikit-learn package was utilized for Non-Negative Matrix Factorization (NMF) analysis, and a custom Python script was developed to generate masks for different components and their corresponding spectra [52]. Rietveld refinement was performed on the spectra to identify the different phases present in the different components. NMF analysis was applied analogously to the PDF-CT data.

XAS Experimental

Mn K-edge X-ray Absorption Near Edge Structure (XANES) measurements were collected on the B18 beamline at Diamond Light Source. Data was collected in fluorescence mode on intact pellets using a QEXAFS setup, with an energy resolution of 0.25 eV, with a fast scanning Si(111) crystal monochromator and a Pt mirror. The *ex situ* samples were undiluted, and run in the "activated" and "used" states. Data was collected over 2 h for each sample. Data was analysed using the Demeter package Athena [53].

µ-XRF Experiments

µ-XRF measurements were performed on the 3% Mn samples before and after the reaction where the cross-section and lateral faces were examined by IXRF (Austin, TX, USA). The X-ray fluorescence (XRF) element mapping was collected using IXRF's Atlas Micro-XRF spectrometer, with a primary polycapillary source (50 W – 50 kV / 1000 µA) that leverages a Rh anode target and is capable of a 5-µm spot size [54]. The source enters the top of the chamber, which allows for the spot to be completely orthogonal with the sample to achieve a true 5-µm spot size. Multiple scans were made of the samples and the focal plane/Z-stage height were set to achieve a 5-µm spot size. The dwell time at each corresponding pixel ranged from 50–200 ms and the samples were scanned under vacuum.

Results

Fischer-Tropsch Performance

The CO conversion and product selectivity for olefins, alcohols and C_{5+} was measured throughout the reaction for 0–270 h and is presented in Fig. 1 as averages for all the samples. The average CO conversion of the 2% Mn sample was the highest (49%) whilst the 1% Mn sample was marginally lower at

46%. This indicates that the Mn promoter improved conversion, even at low weight percentages, possibly due to smaller crystallite size of the FCC/HCP Co phases. However, at increasing Mn loading (5–10 wt. %), conversion was also lower at 36%. The 10% Mn sample which was reduced at 450°C had an average conversion rate at 38% throughout the experiment which was similar to the 0 wt. % sample.

At higher weight percentages of Mn (3–10 wt. %) there was an increase in alcohol and olefin selectivity. The selectivity to olefins and alcohols was highest for the 3% Mn sample. C_{5+} selectivity was the highest for the 1 and 2% Mn catalysts (77–80%) suggesting that the Mn promoted chain growth at low weight percentages. The 1 and 2% Mn catalysts exhibited high C_{5+} selectivity and lower olefin and alcohol selectivity. The 10% Mn catalyst which was reduced at 450°C showed similar selectivity as the 0% Mn catalyst. Catalyst stability was investigated throughout the reaction and the results for the 2% Mn catalyst are presented in Figure S2 where it was found that activity and selectivity was relatively constant from 0–270 h (up to 12 days under FT conditions). Furthermore, Fig. 2 illustrates that the catalytic activity of the pellets remained consistent in a long-term study lasting 1500 h, showcasing the recoverability of the catalysts with resumption of catalytic activity even after shutdown periods.

Mean XRD-CT pattern Refinement

The mean XRD-CT patterns (illustrated in Fig. 3 in the 3.4–4.0 2θ° range) were produced by summing the patterns for all pixels which provided a starting point for analysis. Evidence of the crystalline TiO_2 support is shown through the (111) rutile peak at 3.56°. The anatase TiO_2 polymorph is not present in this range but is evident in the full pattern (Figure S6). A summary of the Rietveld refinement results is presented in Table 1 (complete results in Table S2). It was found that the Co_2C phase increased (peaks at 3.68° and 3.93°) with Mn loading whilst the cobalt metal phases (peak at 3.81°) decreased. The Co was mostly reduced in the Co-containing species as the samples were recovered from the reactor under predominantly reducing conditions and the wax products remaining on the catalysts prevented oxidation. There was, however, a small percentage (3 wt. %) of CoO detected in the 10% Mn sample with an expanded lattice parameter (4.29 Å). A fraction of this could be MnO given that MnO was not separately refined. This is due to Co and Mn having similar scattering factors. Previous research has also pointed towards the presence of mixed-oxide spinels with an expanded lattice parameter ($Co_{1-x}Mn_xO$) [28,55]. Consistent with previous work, no other crystalline Mn-containing species were detected [28]. The mean pattern in Figure S7 highlights the presence of the different Co phases in the 3% Mn sample which contains the Co metal phases (FCC and HCP) and the Co_2C phase as well as the difference between the refined and experimental data. The FCC (200) peak was excluded from the refinements as it was found to have reduced intensity due to the possible presence of stacking faults [56]. Whilst this aided the fit of the FCC (100) peak, the presence of stacking faults results in more complex peak shapes and asymmetry that would require more elaborate modelling to improve the fit further [56]. The full pattern is presented in Figure S6, where the support phases (TiO_2), anatase and rutile, were identified whilst $MnTiO_3$ was formed in the 10% Mn sample reduced at 450°C.

For the 1 and 2% Mn loading samples, less than 1 wt. % of Co_2C phase was present. However, above 3% Mn loading, the wt. % of Co_2C noticeably increased from 3.6 wt. % (3% Mn) to 7.1 wt. % (10% Mn). This increase in Co_2C formation corresponds with increasing alcohol and olefin selectivity of the catalyst. The crystallite size of the Co FCC phase was found to decrease with increasing Mn loading which correlates with previous research [57]. This smaller crystallite size in the 1 and 2% Mn samples was a likely cause for the increased activity and C_{5+} selectivity in these samples. The total Co metal (FCC + HCP + Co_2C) wt. % was found to be approximately 8 wt. % (lower than the known 10 wt. %) indicating that some of the Co was not found in the XRD data due to small crystallite sizes or disordered Co being present. The low wt. % (0.5-2%) of CoO present and the retention of Co_2C phase affirm the efficacy of the catalyst wax passivation method.

A 5% Mn sample was extracted after 150 h of reaction, and it was found that the Co_2C phase had already formed at this intermediate stage. The refined weight percentage of the Co_2C phase increased from 7.5 wt. % at 150 h to 8.9 wt. % at 300 h and the crystallite size increased from 7.5 nm to 9.3 nm. The data indicates that carbide had already become the dominant Co phase by 150 h with only marginal further increase observed until 300 h for the samples. This data only shows the bulk average analysis across the samples, akin to the analysis from a laboratory X-ray diffractometer study, where an increase in overall Co_2C was found with increasing Mn loading. Using this data in combination with XRD-CT analysis enables not just a bulk analysis to be performed but also spatially resolved phase and particle size correlation.

Table 1

Rietveld Refinement results of the XRD-CT mean patterns illustrating the Co phase wt. % and CS (crystallite size in nm) in the samples extracted after 150 and 300 h. The Co_2C wt. % increases with Mn loading whilst the Co metal phases (FCC and HCP) decrease with increasing Mn wt. % beyond 5%. The 10 wt. % samples were reduced at 450°C.

		Mn wt. %							
Time (h)		**150**	**300**						
Phase		**5%**	**0%**	**1%**	**2%**	**3%**	**5%**	**10%**	**10%[a]**
Co_2C	Wt. %	7.5	-	0.6	0.9	3.6	8.9	7.1	-
	CS	7.5	-	-	6.5	10.6	9.3	11.7	-
FCC	Wt. %	0.4	3.5	3.3	3.6	1.6	0.1	0.0	2.9
	CS	3.54	10.5	8.1	7.7	5.2	-	-	11.2
HCP	Wt. %	0.2	4.9	4.8	3.8	3.1	0.2	0.7	5.3
	CS	-	2.6	2.2	2.2	7.1	-	9.9	2.9

[a] Reduction at 450 °C

XRD-CT Refinement

The XRD-CT spatial mappings presented in Fig. 4 illustrate the weight percentages of the different phases present in the catalyst and their crystallite size with spatial resolution. At lower Mn loadings, Co metal (in both FCC and HCP phases) is uniformly distributed, while at higher loadings, it tends to concentrate towards the centre of the extrudates. This spatial distribution is further elucidated in Fig. 5, which displays XRD patterns of consecutive layers within the 3% Mn catalyst. Here, the Co_2C phase predominates at the periphery of the extrudates, while FCC and HCP Co metal phases are concentrated at the core. The 3% Mn sample exhibits the highest concentration of the Co HCP phase (7–8 wt. %) compared to the 0–2% Mn samples (3–4 wt. %) at the central region of the extrudates, evident in the XRD patterns of the successive layers in Figure S8. This observation was not captured in the analysis of the mean XRD patterns, where lower HCP content was found for the 3% Mn sample. This highlights the efficacy of the XRD-CT technique in detecting phase distribution heterogeneities, revealing distinctions between bulk and specific regions. Notably, the 3% Mn sample represents the point just before the significant formation of Co_2C and an increase in the HCP phase. This suggests an equilibrium between cobalt carburization and reduction back to HCP cobalt, favouring the latter during the reduction process due to their structurally similar hexagonal configuration. Above this equilibrium point in Mn loading, cobalt carbide phase predominates, while below it, the HCP phase prevails. Strikingly, the 3% Mn sample also exhibited the highest alcohol and olefin selectivity, signifying that an optimal equilibrium between the HCP and Co_2C phases was reached in this sample, contributing to an enhanced selectivity towards oxygenates.

FCC and HCP Co phases were both present in the 10% Mn (reduced at 450°C) sample and there was no presence of carbides, exhibiting a similar distribution of phases as the 0% Mn sample. Both catalysts also exhibited low selectivity for alcohols and olefins. This is due to the Mn being locked away in the Mn titanate phase which prevents its promotional effects that require the Mn to be close to the cobalt [58]. Only a small percentage of CoO was found in the samples indicating that most of the cobalt was reduced however more was found to be present at higher Mn loadings, likely due to the presence of mixed oxide spinels ($Co_{1-x}Mn_xO$). The R_{wp} (residual weight percentage) was relatively constant at around 7–8% indicating a good fit for all the patterns.

Like in the mean refinements, it was found that the FCC crystallite size decreases with increasing Mn loading which corresponds to previous research [28]. The crystallite sizes of the HCP phase (2.5 nm) are much smaller than the FCC phase (6–10 nm) except for the 3% Mn catalyst where larger HCP particles were found to be formed at the centre of the extrudates. Larger Co_2C particles (14 nm) are found to be formed on the periphery of the 3% Mn catalyst compared to the 5 and 10% Mn catalysts (10 nm). This further supports the hypothesis of a Co_2C to HCP phase transformation equilibrium. This also agrees with previous research that found that Mn in close proximity to larger cobalt particles would carburize [59]. Small CoO crystallites were found to be present at higher Mn loadings (5 and 10 wt. %), which were

expected to be mixed-oxide spinels ($Co_{1-x}Mn_xO$), indicating that the Mn inhibited reduction of Co. The phase distribution and crystallite sizes did not vary significantly along the length of the pellet and XRD-CT cross-section maps of the samples at alternative positions within the pellets are presented in Figure S10.

Spatial maps of the wax were produced (Fig. 6) by refining polyethylene $(C_3H_6)_n$ and it was found that that more wax content remained on the catalyst with increasing Mn loading. This correlates with research that found that olefin products are more likely to re-adsorb on the catalyst surface, due to greater solubility in synthesis liquids, and undergo secondary reactions such as hydrogenation [60,61].

NMF Analysis of XRD-CT data

NMF analysis was performed to ensure a thorough identification of all phases present in the catalyst. The analysis revealed the presence of five components as further increasing the component count led to the inclusion of components that resembled noise. Due to the homogeneous presence of the support and crystalline wax $(C_3H_6)_n$, all components included these phases. In Figure S11, masked images display the component locations, while Figure S12 illustrate the computed XRD patterns of the components and Table S4 contains the Rietveld refinement results. Component 1 (FCC/HCP phases) was concentrated at the catalyst centre with higher Mn loading, while Component 3 (Co_2C) was primarily located on the catalyst periphery, consistent with the XRD-CT findings. Furthermore, component 2 was found to contain the $MnTiO_3$ phase which was found only in the 10% Mn catalyst reduced at 450°C. Components 4 and 5, demonstrated a co-location of HCP and Co_2C phases but only accounted 2.4 and 0.3 wt. % of the data intensity respectively. The NMF analysis confirmed that no additional phases were present that were not detected by the XRD-CT analysis.

PDF-CT data analysis

The summed PDF patterns were produced by summing all the Bragg data for each pixel and then Fourier transforming the result. Real-space refinement was performed on the patterns and the results are presented in Table S6. The refined mean patterns from 0–10 Å are presented in Fig. 7 where there are changes to the Co-Co peak at 2.5 Å with increasing Mn due to the formation of cobalt carbide. Similar to the XRD refinement, the PDF results indicated increased Co_2C formation with increasing Mn loading, first appearing at 3% Mn, whilst Co (FCC and HCP) phases were present at lower Mn loadings (0 and 1 wt. %). There was a higher percentage of FCC/HCP cobalt detected in the PDF than in the XRD indicating the presence of small cobalt metal particles. A larger percentage of CoO is detected for the 10% Mn sample indicating that the Mn was present in small mixed-oxide spinels ($Co_1Mn_{1-x}O$) or small MnO particles (1 nm) that could not be detected by XRD. Previous research has also found that small Co particles oxidise to CoO [38].

The PDF-CT wt% and crystallite size maps are presented in Fig. 8. The results from the PDF-CT refinement were consistent with the findings from the XRD-CT refinement where an increasing Mn loading led to an increase in Co_2C formation on the extrudate periphery and decreasing Co (FCC and HCP) content in the centre. Similar to the XRD results, the crystallite size of the FCC particles was found to

decrease with increasing Mn loading, correlating with previous research [28]. A higher HCP wt. % was found in the centre of the extrudates at higher Mn loadings with the highest concentration present in the 3% Mn sample. This aligns with the XRD results, revealing a phase equilibrium between the Co_2C and HCP phases, with the Co_2C phase prevailing at elevated Mn loading levels.

NMF analysis was also performed on the PDF-CT data to ensure that all phases including non-crystalline phases were detected. The spectra were decomposed into 5 components although only 3 were significant. Two of the components (2 and 4) were of much weaker intensity comprising only 0.1–0.2 wt. % of the total intensity. The component locations are shown in Figure S14 and their respectives PDFs are illustrated in Figure S15 while Table S8 contains the Rietveld refinement results. Component 1 contained FCC/HCP Co located at the centre of the pellets at higher Mn loading with the presence of small CoO nanoparticles. Component 5 contained the Co_2C phase that was present on the periphery in the 3–10% Mn samples. Component 3 contained the $MnTiO_3$ phase co-located with FCC/HCP Co which was exclusively present in the 10% Mn sample reduced at 450°C. The NMF analysis confirmed the previous PDF-CT results serving as an efficient tool for spatial decomposition of PDF-CT data into its constituent chemical components.

XRF mapping experiments

µ-XRF images are presented in Figure S16 which provide a visual insight into the cross-sections and lateral faces of the 3% Mn samples both before and after undergoing a 300 h reaction. The images reveal that Mn and Co are colocated in the samples and there are no significant alterations in their distribution observed before and after the extended reaction period. This opposes recent research that found that Mn Oxide and Co were mobile under reaction conditions [59].

XAS Results

To understand how the environment of the Mn species in the catalysts varied with different weight loadings, X-ray Absorption Near Edge Structure (XANES) were collected of the Mn K-edge and compared to a variety of oxidic standards (Fig. 9).

All systems shared a common pre-edge feature at 6540 eV, which is attributed to electronic transitions from the 1s to 3d levels. This feature however is known to be largely insensitive to the precise environment compared to the main-edge feature [62]. Similarly, there is a significant feature at 6560 eV, attributed to dipole-allowed 1s to 4p transitions, which is particularly pronounced in the 1–2% Mn samples [63]. The XANES data shows excellent agreement with the 1–2% Mn samples (Fig. 9, red and blue respectively), suggesting they are in very similar environments. However, as the loading increases, in the main-edge (between 6545 and 6550 eV), there is a notable shift to lower energies, as the Mn weight loading increases, suggesting a reduction in oxidation state. Comparing these spectra with known reference compounds (MnO, MnO_2, Mn_3O_4, Mn_2O_3 and $MnTiO_3$), Figure S17 shows that the 1–2% Mn systems have a strong resemblance to Mn_3O_4 and Mn_2O_3 (Figure S17A). This suggests that at least part of the Mn in these catalytic systems are Mn^{3+} in an octahedral environment. The pre-edge peak in the 1

and 2 wt. % however is around 1 eV slightly lower than the Mn_3O_4 and Mn_2O_3 species, this is likely due to a slightly lower average oxidation states in the samples, compared to the oxidic references, or due to their existence as smaller nanoparticles, and not bulk oxides. Above these loadings (> 2 wt. % Mn, Figure S17B) a signal at 6553 eV begins to evolve, which coincides with the main feature in the reference MnO spectra. The 10% Mn sample reduced at 450°C presented similar features to the $MnTiO_3$ reference, suggesting that post-reaction the Mn active sites alloy with the TiO_2 support, forming a ternary phase. Overall, the XANES study suggests that at lower weight loadings (1–2% Mn) the Mn environment resembles Mn_3O_4 and Mn_2O_3. At higher weight loadings (3–10% Mn) there are significant features from MnO appearing, showing a notable change from the Mn_3O_4 and Mn_2O_3 environment.

Summary and Conclusions

μ-XRD-CT and μ-PDF-CT (or XRS-CT) techniques were used as complementary techniques to study Co/TiO_2/Mn FT catalysts recovered after reaction which maintained their state due to *in situ* wax passivation. The protective wax coating product preserved the chemical integrity of the extrudates enabling the X-ray scattering experiments to be conducted after the retrieval of the catalysts following the reaction. This preservation enabled the study of the state of the active catalyst at realistic reaction durations (300 h), a feasibility that was previously constrained in the context of time-limited *in situ* synchrotron experiments and demonstrates the feasibility of this approach for characterising spent FT catalysts to understand active states and deactivation phenomena in the future.

It was found that increasing Mn loading led to the formation of increasing amounts of MnO which correspondingly led to increasing cobalt carbide content and decreasing cobalt metal (FCC and HCP) in the reacted catalysts. The cobalt carbide was located on the periphery of the catalytic extrudates whilst the cobalt metal phases (FCC and HCP) were at the centre. This could be due to a higher partial pressure of CO at the periphery due to pore diffusion limitations of the syngas. Previous research demonstrated that Co_2C is formed inversely proportionally to the H_2/CO ratio [22]. Evidence has also shown that before reduction, aggregated cobalt oxide particles (weak metal-support interactions) which are preferably located at the edges of the extrudates reduce more quickly [38]. This was suggested due to a higher H_2 concentration at the centre and particle size effects. A sudden increase in alcohol and olefin selectivity at 3% Mn coincided with an increased amount of Co_2C and the highest HCP concentration indicating that an optimum equilibrium was reached between the two phases. The presence of the two phases contributed synergistically to achieve maximum oxygenate selectivity. It is thought that the increased Mn leads to a decrease of the CO dissociation barrier promoting carburisation of cobalt [28]. XANES analysis revealed that the Mn was oxidic and increasing MnO was present at higher weight loadings (3–10 wt. % Mn) which correlated with increasing olefin and alcohol selectivity. Previous research has found that dissociation is more likely to occur on MnO than Mn_3O_4 [32,64]. Additionally, DFT calculations have found that Co_2C promotes CO non-dissociative adsorption leading to increased oxygenate selectivity [26]. XRF

imaging of the extrudates revealed that there was no detectable change in the sample Co/Mn distribution under reaction conditions.

The production of Mn titanates ($MnTiO_3$), due to reduction at 450°C, changes the selectivity of the high loading 10% Mn catalyst to that of a 0% Mn catalyst, where there is a higher C_{5+} but lower olefins and alcohol selectivity. The Mn is locked away in Mn titanates and is not able to promote cobalt carbide formation leaving the cobalt metal in the FCC and HCP form.

PDF analysis, which does not assume periodic order, allowed the study of small nanoparticles and disordered phases that were not detectable using XRD. PDF-CT revealed the presence of small CoO particles (~ 1 nm) in the 10% Mn sample indicating the presence of mixed oxide spinels ($Co_xMn_{1-x}O$). This suggests that Mn inhibits Co reduction which led to decreased CO conversion and product yield. Higher FCC/HCP Co wt. % was found using PDF indicating that a small proportion was present as small nanoparticles that could not be detected in the XRD refinements. NMF analysis was used as an efficient tool to spatially decompose the XRD-CT and PDF-CT data into different chemical components ensuring the detection of all phases.

Recovering and imaging the catalyst after 300 h of reaction provided an insight into the catalytic structure during industrially relevant conditions and timescales. Increasing Co_2C content was detected with increasing Mn loading which correlated with increasing alcohol and olefin selectivity. Spatial resolution of the phases within the extrudates was provided by using XRD-CT and PDF-CT chemical imaging techniques. Further research is required to uncover more details regarding the specific role of Mn and potential reactions mechanisms contributing to the increased formation of olefins and oxygenates with increasing Co_2C content.

Declarations

Acknowledgements

The authors would like to express their gratitude to staff at ID 31, ESRF, for beamline access and specifically, Helen Isern and Florian Russello who helped with experiment preparation. Appreciation is also expressed to the UK Catalysis Hub and B18, Diamond Light Source, for access to Block Allocation Group (SP29271-7). BP and EPSRC are thanked for an iCASE award to DF. EPSRC are also thanked for funding for the UK Catalysis Hub via grant EP/R026939/1.

Competing interests statement

Andrew M. Beale is an equal shareholder and Chief Scientific Officer of Finden Ltd.

DOI of raw data: 10.15151/ESRF-ES-659393071

References

1. Vosoughi, V., Badoga, S., Dalai, A. K. & Abatzoglou, N. Modification of mesoporous alumina as a support for cobalt-based catalyst in Fischer-Tropsch synthesis. *Fuel Processing Technology* **162**, 55-65 (2017).
2. Fischer, F. & Tropsch, H. Uber die Herstellung synthetischer olgemische (Synthol) durch Aufbau aus Kohlenoxyd und Wasserstoff. *Brennst. Chem* **4**, 276-285 (1923).
3. Choi, Y. H. *et al.* Carbon dioxide Fischer-Tropsch synthesis: A new path to carbon-neutral fuels. *Applied Catalysis B: Environmental* **202**, 605-610, (2017).
4. *HyCOgen and FT CANS, Innovative Technologies to Enable Sustainable Fuel Production Selected for Repsol and Aramco's Synthetic Fuel Plant in Bilbao*, <https://matthey.com/products-and-markets/chemicals/catacel-ssr-catalyst> (2022).
5. Jeske, K. *et al.* Direct conversion of syngas to higher alcohols via tandem integration of Fischer–Tropsch synthesis and reductive hydroformylation. *Angewandte Chemie* **134**, e202201004 (2022).
6. Martinelli, M., Gnanamani, M. K., LeViness, S., Jacobs, G. & Shafer, W. D. An overview of Fischer-Tropsch Synthesis: XtL processes, catalysts and reactors. *Applied Catalysis A: General* **608**, 117740 (2020).
7. Dancuart, L. & Steynberg, A. in *Studies in surface science and catalysis* Vol. 163 379-399 (Elsevier, 2007).
8. Font Freide, J. J. *et al.* An adventure in catalysis: the story of the BP Fischer–Tropsch catalyst from laboratory to full-scale demonstration in Alaska. *Topics in catalysis* **26**, 3-12 (2003).
9. Overtoom, R., Fabricius, N. & Leenhouts, W. in *Proceedings of the 1st Annual Gas Processing Symposium.* 378-386 (Elsevier).
10. Peacock, M. *et al.* Innovation in Fischer–Tropsch: developing fundamental understanding to support commercial opportunities. *Topics in Catalysis* **63**, 328-339 (2020).
11. *Johnson Matthey and bp to support planned production of carbon negative renewable diesel fuel plant at Strategic Biofuels project in Louisiana*, <https://matthey.com/jm-and-bp-strategic-biofuels-project> (2023).
12. Liu, J.-X., Su, H.-Y., Sun, D.-P., Zhang, B.-Y. & Li, W.-X. Crystallographic Dependence of CO Activation on Cobalt Catalysts: HCP versus FCC. *Journal of the American Chemical Society* **135**, 16284-16287, doi:10.1021/ja408521w (2013).
13. Ducreux, O., Lynch, J., Rebours, B., Roy, M. & Chaumette, P. In situ characterisation of cobalt based Fischer-Tropsch catalysts: A new approach to the active phase. *Studies in surface science and catalysis*, 125-130 (1998).
14. Enache, D. I., Rebours, B., Roy-Auberger, M. & Revel, R. In situ XRD study of the influence of thermal treatment on the characteristics and the catalytic properties of cobalt-based Fischer–Tropsch catalysts. *Journal of Catalysis* **205**, 346-353 (2002).
15. De la Peña, O. S. VA; Homs, N.; Fierro, JLG; Ramírez de la Piscina, P. *Catal. Today* **114**, 422 (2006).

16. Karaca, H. *et al.* Structure and catalytic performance of Pt-promoted alumina-supported cobalt catalysts under realistic conditions of Fischer–Tropsch synthesis. *Journal of catalysis* **277**, 14-26 (2011).
17. Gnanamani, M. K., Jacobs, G., Shafer, W. D. & Davis, B. H. Fischer–Tropsch synthesis: Activity of metallic phases of cobalt supported on silica. *Catalysis Today* **215**, 13-17, (2013).
18. Ducreux, O., Rebours, B., Lynch, J., Roy-Auberger, M. & Bazin, D. Microstructure of supported cobalt Fischer-Tropsch catalysts. *Oil & Gas Science and Technology-Revue de l'IFP* **64**, 49-62 (2009).
19. Weller, S., Hofer, L. & Anderson, R. The role of bulk cobalt carbide in the Fischer—Tropsch synthesis. *Journal of the American Chemical Society* **70**, 799-801 (1948).
20. van Ravenhorst, I. K. *et al.* On the Cobalt Carbide Formation in a Co/TiO2 Fischer–Tropsch Synthesis Catalyst as Studied by High-Pressure, Long-Term Operando X-ray Absorption and Diffraction. *ACS Catalysis* **11**, 2956-2967, (2021).
21. Du, H. *et al.* Study on CaO-promoted Co/AC catalysts for synthesis of higher alcohols from syngas. *Fuel* **182**, 42-49 (2016).
22. Claeys, M. *et al.* In situ magnetometer study on the formation and stability of cobalt carbide in Fischer–Tropsch synthesis. *Journal of catalysis* **318**, 193-202 (2014).
23. Zhong, L. *et al.* Cobalt carbide nanoprisms for direct production of lower olefins from syngas. *Nature* **538**, 84-87, (2016).
24. Zhao, Z. *et al.* Insight into the Formation of Co@Co2C Catalysts for Direct Synthesis of Higher Alcohols and Olefins from Syngas. *ACS Catalysis* **8**, 228-241, (2018).
25. Anton, J. *et al.* The effect of sodium on the structure–activity relationships of cobalt-modified Cu/ZnO/Al2O3 catalysts applied in the hydrogenation of carbon monoxide to higher alcohols. *Journal of Catalysis* **335**, 175-186 (2016).
26. Pei, Y.-P. *et al.* High alcohols synthesis via Fischer–Tropsch reaction at cobalt metal/carbide interface. *ACS Catalysis* **5**, 3620-3624 (2015).
27. Morales, F., Weckhuysen, B. M., Spivey, J. & Dooley, K. Promotion effects in Co-based Fischer-Tropsch catalysis. *Catalysis* **19**, 1-40 (2006).
28. Paterson, J. *et al.* Elucidating the Role of Bifunctional Cobalt-Manganese Catalyst Interactions for Higher Alcohol Synthesis. *European Journal of Inorganic Chemistry* **2020**, 2312-2324, (2020).
29. Pedersen, E. Ø., Svenum, I.-H. & Blekkan, E. A. Mn promoted Co catalysts for Fischer-Tropsch production of light olefins – An experimental and theoretical study. *Journal of Catalysis* **361**, 23-32, (2018).
30. Johnson, G. R., Werner, S. & Bell, A. T. An investigation into the effects of Mn promotion on the activity and selectivity of Co/SiO2 for Fischer–Tropsch synthesis: evidence for enhanced CO adsorption and dissociation. *ACS Catalysis* **5**, 5888-5903 (2015).
31. Lebarbier, V. M. *et al.* Effects of La2O3 on the mixed higher alcohols synthesis from syngas over Co catalysts: a combined theoretical and experimental study. *The Journal of Physical Chemistry C* **115**,

17440-17451 (2011).

32. Zhu, Y. *et al.* Role of Manganese Oxide in Syngas Conversion to Light Olefins. *ACS Catalysis* **7**, 2800-2804, (2017).
33. Salazar-Contreras, H. G., Martínez-Hernández, A., Boix, A. A., Fuentes, G. A. & Torres-García, E. Effect of Mn on Co/HMS-Mn and Co/SiO2-Mn catalysts for the Fischer-Tropsch reaction. *Applied Catalysis B: Environmental* **244**, 414-426, (2019).
34. Bagheri, S., Muhd Julkapli, N. & Bee Abd Hamid, S. Titanium Dioxide as a Catalyst Support in Heterogeneous Catalysis. *The Scientific World Journal* **2014**, 727496, (2014).
35. Storsæter, S., Tøtdal, B., Walmsley, J. C., Tanem, B. S. & Holmen, A. Characterization of alumina-, silica-, and titania-supported cobalt Fischer–Tropsch catalysts. *Journal of Catalysis* **236**, 139-152 (2005).
36. Murzin, D. Y. *Engineering catalysis*. (Walter de Gruyter GmbH & Co KG, 2020).
37. De Jong, K. P. *Synthesis of solid catalysts*. (John Wiley & Sons, 2009).
38. Senecal, P. *et al.* Real-Time Scattering-Contrast Imaging of a Supported Cobalt-Based Catalyst Body during Activation and Fischer–Tropsch Synthesis Revealing Spatial Dependence of Particle Size and Phase on Catalytic Properties. *ACS Catalysis* **7**, 2284-2293, (2017).
39. Price, S. W. T. *et al.* Chemical imaging of Fischer-Tropsch catalysts under operating conditions. *Science Advances* **3**, e1602838, (2017).
40. Omori, N. E., Bobitan, A. D., Vamvakeros, A., Beale, A. M. & Jacques, S. D. Recent developments in X-ray diffraction/scattering computed tomography for materials science. *Philosophical Transactions of the Royal Society A: Mathematical, Physical and Engineering Sciences* **381**, 20220350 (2023).
41. Basile, F. *et al.* Combined Use of Synchrotron-Radiation-Based Imaging Techniques for the Characterization of Structured Catalysts. *Advanced Functional Materials* **20**, 4117-4126, (2010).
42. Partington, R., Clarkson, J., Paterson, J., Sullivan, K. & Wilson, J. Quantitative carbon distribution analysis of hydrocarbons, alcohols and carboxylic acids in a Fischer-Tropsch product from a Co/TiO 2 catalyst during gas phase pilot plant operation. *Journal of Analytical Science Technology* **11**, 1-20 (2020).
43. *hte provides high throughput unit for syngas conversion to bp*, <https://www.hte-company.com/en/news-events/news/news-with-bp-1> (2023).
44. Vamvakeros, A. *et al.* Interlaced X-ray diffraction computed tomography. *Journal of Applied Crystallography* **49**, 485-496, (2016).
45. Ashiotis, G. *et al.* The fast azimuthal integration Python library: pyFAI. *Journal of Applied Crystallography* **48**, 510-519 (2015).
46. Vamvakeros, A. *et al.* Removing multiple outliers and single-crystal artefacts from X-ray diffraction computed tomography data. *Journal of Applied Crystallography* **48**, 1943-1955 (2015).
47. MATLAB Version: 9.7.0 (R2020b) (The MathWorks Inc., Natick, Massachusetts, 2020).

48. Coelho, A. A. TOPAS and TOPAS-Academic: an optimization program integrating computer algebra and crystallographic objects written in C++. *Journal of Applied Crystallography* **51**, 210-218 (2018).
49. Yang, L., Juhás, P., Terban, M. W., Tucker, M. G. & Billinge, S. J. Structure-mining: screening structure models by automated fitting to the atomic pair distribution function over large numbers of models. *Acta Crystallographica Section A: Foundations and Advances* **76**, 395-409 (2020).
50. Dinnebier, R. E., Leineweber, A. & Evans, J. S. in *Rietveld Refinement* 253-268 (De Gruyter, 2018).
51. Lee, D. D. & Seung, H. S. Learning the parts of objects by non-negative matrix factorization. *Nature* **401**, 788-791 (1999).
52. Pedregosa, F. *et al.* Scikit-learn: Machine learning in Python. *the Journal of machine Learning research* **12**, 2825-2830 (2011).
53. Ravel, B. & Newville, M. ATHENA, ARTEMIS, HEPHAESTUS: data analysis for X-ray absorption spectroscopy using IFEFFIT. *Journal of synchrotron radiation* **12**, 537-541 (2005).
54. Williams, B. in *SPIE Conference 12698.*
55. Liu, S. *et al.* The role of intermediate Co x Mn 1− x O (x= 0.6–0.85) nanocrystals in the formation of active species for the direct production of lower olefins from syngas. *Chemical Communications* **55**, 6595-6598 (2019).
56. Sławiński, W. A., Zacharaki, E., Fjellvåg, H. & Sjåstad, A. O. Structural Arrangement in Close-Packed Cobalt Polytypes. *Crystal Growth & Design* **18**, 2316-2325, (2018).
57. Paterson, J. *et al.* Manipulation of Fischer-Tropsch Synthesis for Production of Higher Alcohols Using Manganese Promoters. *ChemCatChem* **10**, 5154-5163, (2018).
58. Paterson, J. *et al.* Controlling cobalt Fischer–Tropsch stability and selectivity through manganese titanate formation. *Catalysis Science Technology* **13**, 3818-3827, (2023).
59. van Koppen, L. M., Dugulan, A. I., Bezemer, G. L. & Hensen, E. J. Sintering and carbidization under simulated high conversion on a cobalt-based Fischer-Tropsch catalyst; manganese oxide as a structural promotor. *Journal of Catalysis* **413**, 106-118 (2022).
60. Iglesia, E., Reyes, S. C. & Madon, R. J. Transport-enhanced α-olefin readsorption pathways in Ru-catalyzed hydrocarbon synthesis. *Journal of Catalysis* **129**, 238-256 (1991).
61. Iglesia, E. Design, synthesis, and use of cobalt-based Fischer-Tropsch synthesis catalysts. *Applied Catalysis A: General* **161**, 59-78, (1997).
62. Farges, F. Ab initio and experimental pre-edge investigations of the Mn K-edge XANES in oxide-type materials. *Physical review B* **71**, 155109 (2005).
63. Kwon, O.-S., Kim, M.-S. & Kim, K.-B. A study on the effect of lithium insertion–extraction on the local structure of lithium manganese oxides using X-ray absorption spectroscopy. *Journal of power sources* **81**, 510-516 (1999).
64. Li, Y. *et al.* Activation of CO over ultrathin manganese oxide layers grown on Au (111). *ACS Catalysis* **11**, 849-857 (2021).

Figures

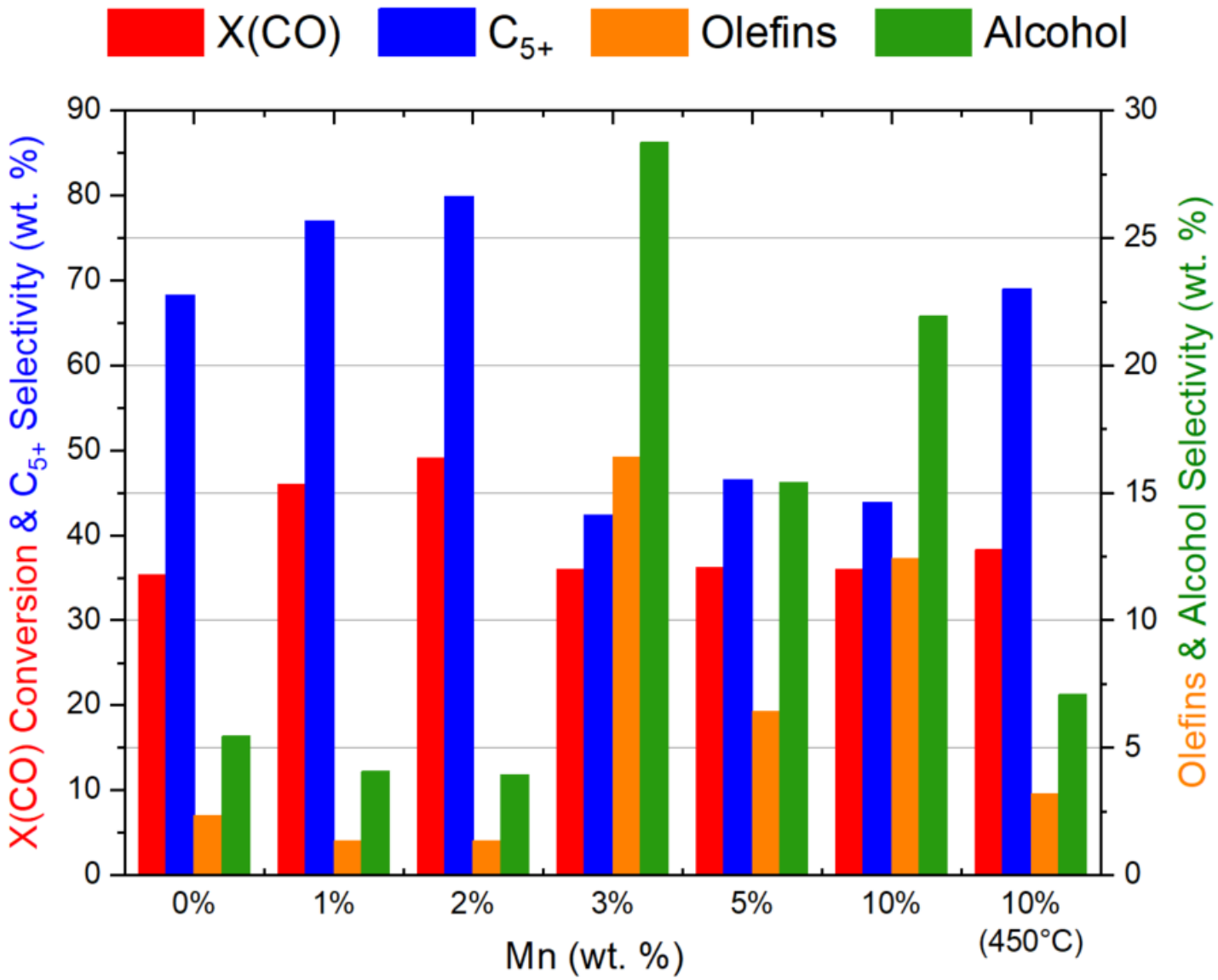

Figure 1

CO conversion and C_{5+}, alcohol and olefin selectivity as a function of Mn loading. It was found that an increase in Mn (wt. %) results in an increase in C_{5+} selectivity from 0-2 wt. %, and increased alcohol and olefin selectivity at > 3 % Mn except for the 10 % Mn sample reduced at 450 °C.

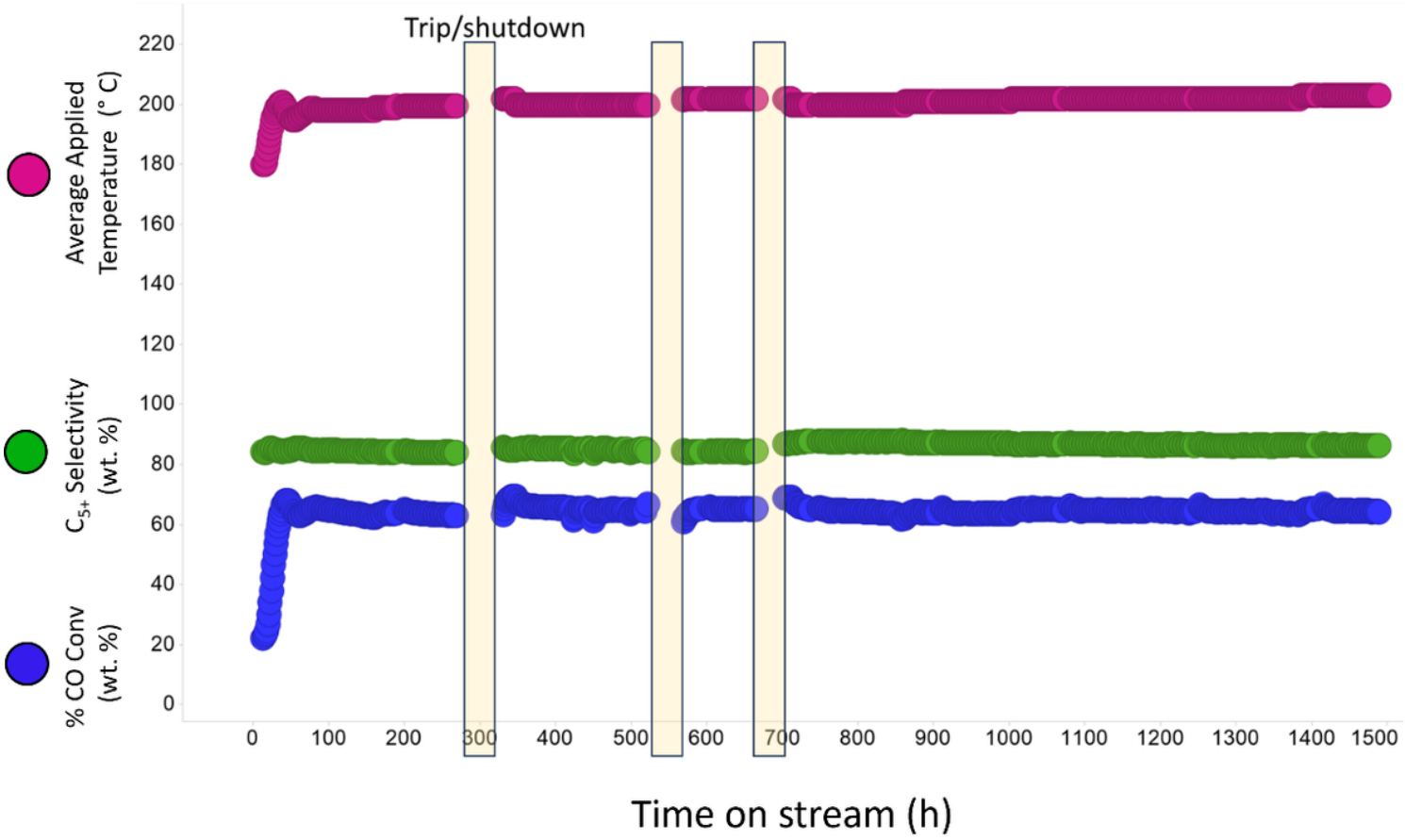

Figure 2

Long-term study of catalyst performance over 1500 h, revealing the stability of the catalytic pellets. The catalysts had consistent CO conversion and C_{5+} selectivity despite three shutdown events.

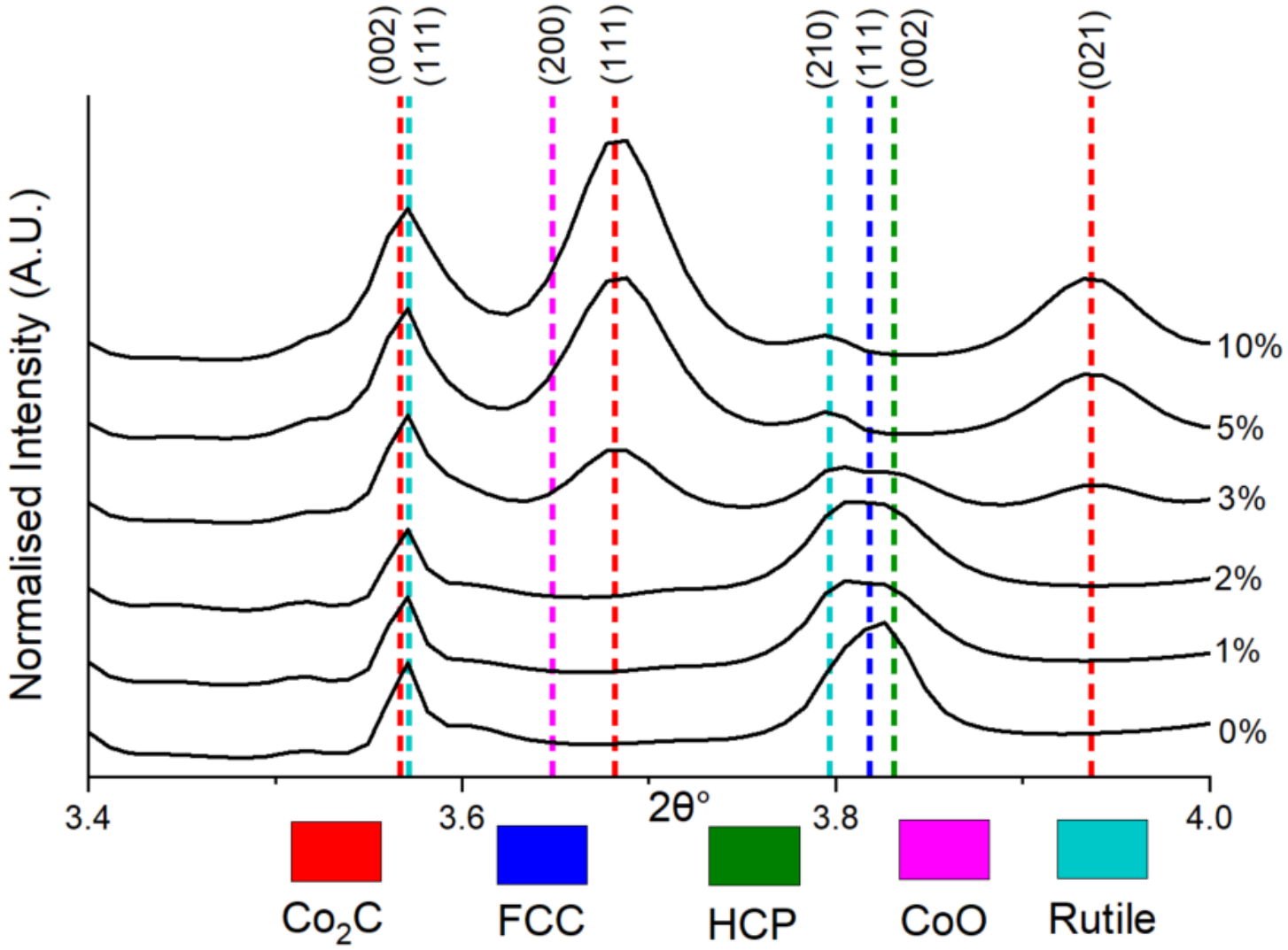

Figure 3

Stacked mean XRD-CT patterns of all the different samples with varied Mn loading (labelled on right) showing the increasing Co_2C content with increasing Mn loading and the concomitant loss of the Co metal phases (FCC and HCP). Low wt. % of CoO was present in the higher Mn loading samples (5 and 10 % Mn). Note that no reflections due to the anatase TiO_2 polymorph are present in this portion of the diffraction pattern.

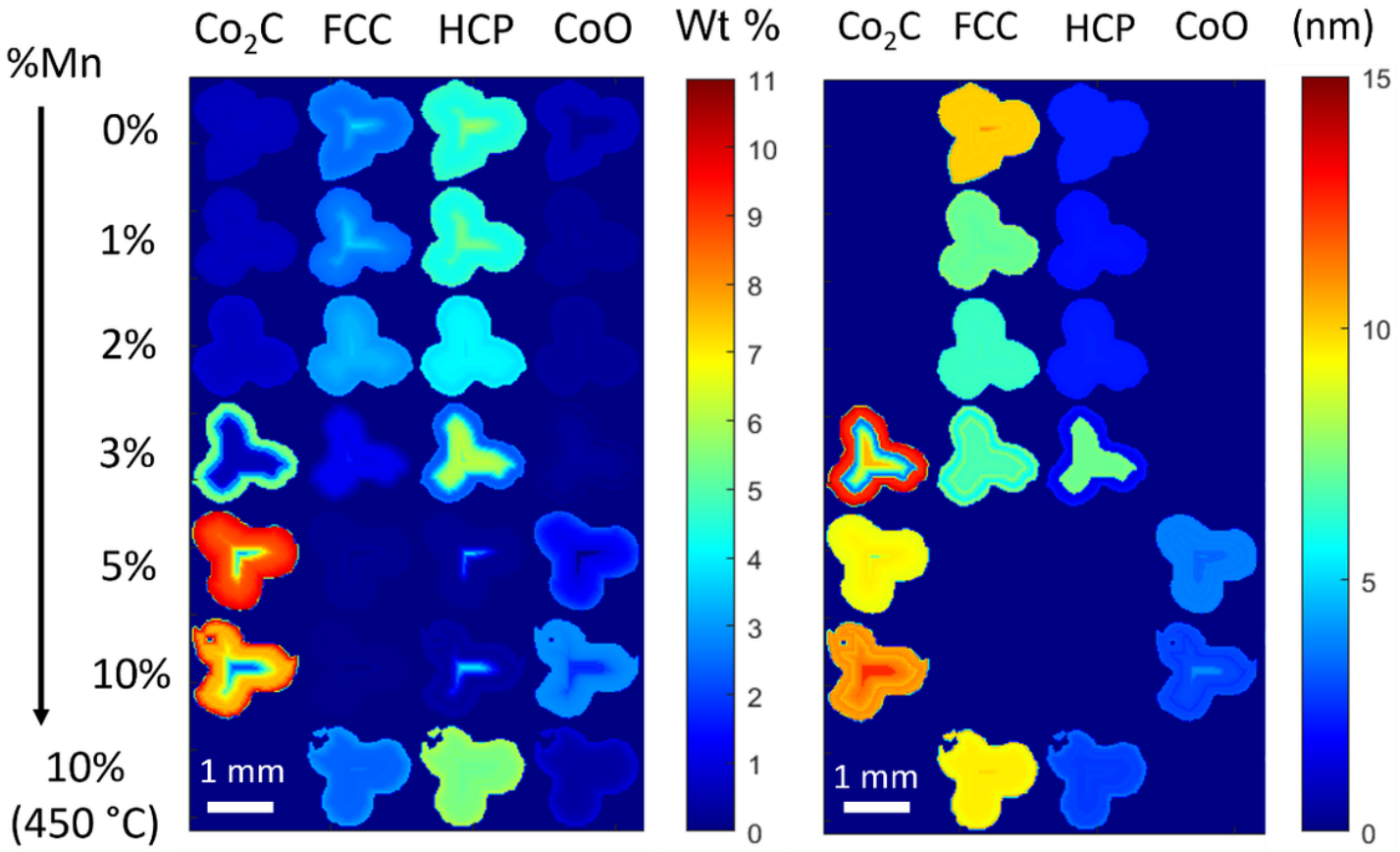

Figure 4

Reconstructed XRD-CT 2D images of the catalytic pellets (extracted after 300 h) illustrating the refined wt. % percentage (left) and crystallite size (right) of the different phases present. Increased Mn loading resulted in more cobalt carbide and a smaller particle size of the FCC phase. Lower Mn loadings had a higher presence of FCC and HCP phases. An egg-shell distribution is observed with Co_2C egg-white and HCP in the centre.

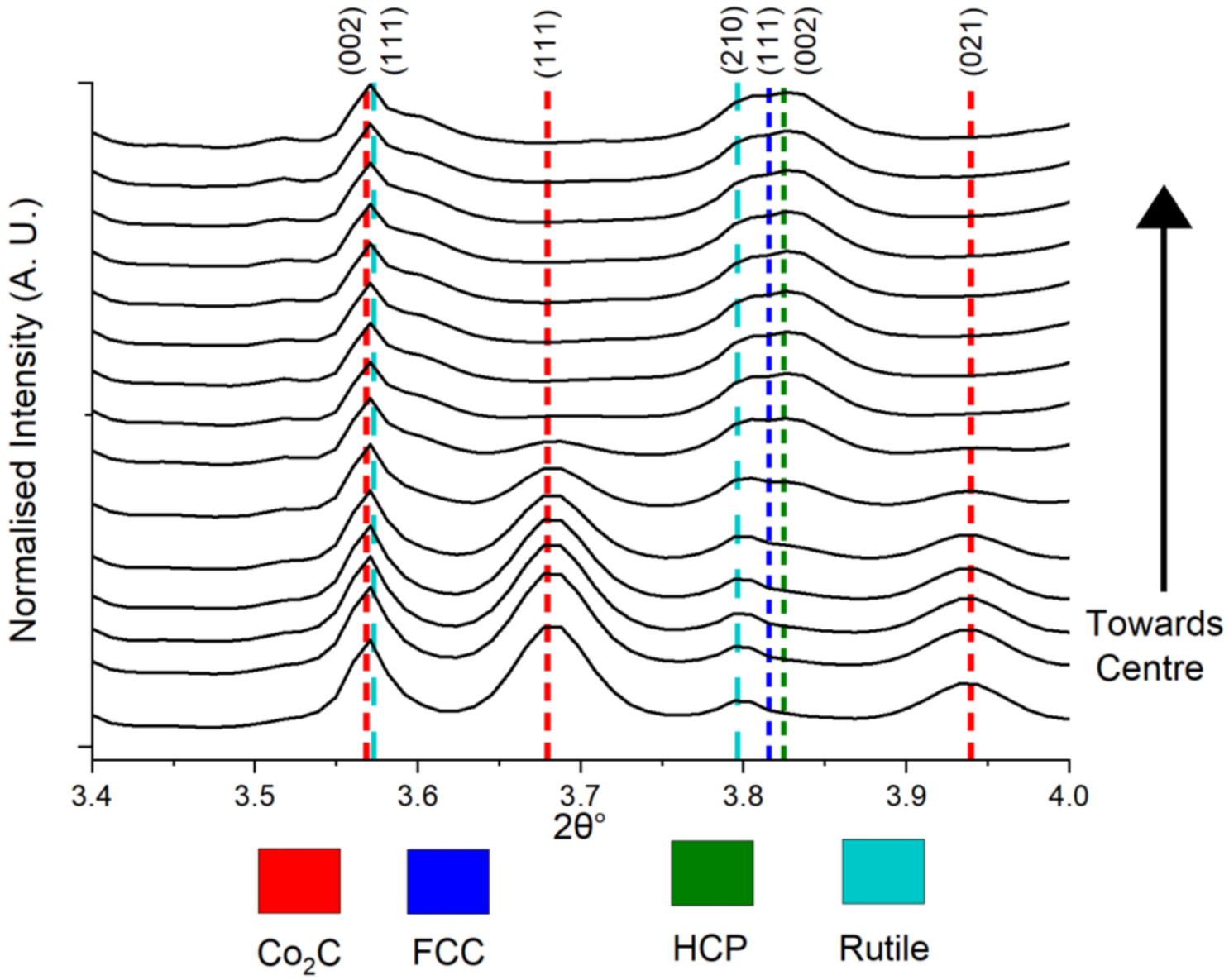

Figure 5

Stacked XRD patterns of the successive layers of the 3 % Mn catalyst extrudate showing the evolution of the different cobalt phases with increasing distances (20 μm steps) from the centre of the catalyst pellet. Co_2C is present at the surface periphery whilst FCC and HCP phases are present at the centre.

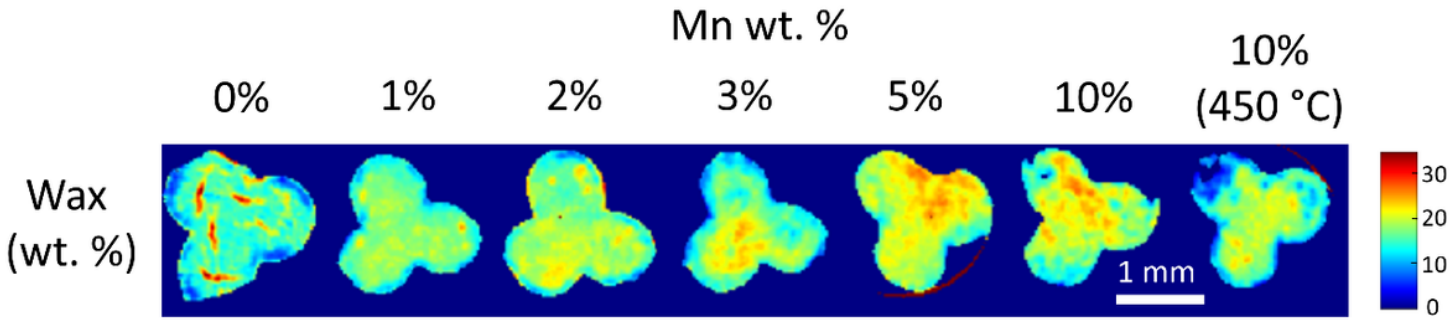

Figure 6

XRD-CT maps of the refined wax $(C_3H_6)_n$ content (wt. %) where increasing wt. % of wax was found at higher Mn wt. %.

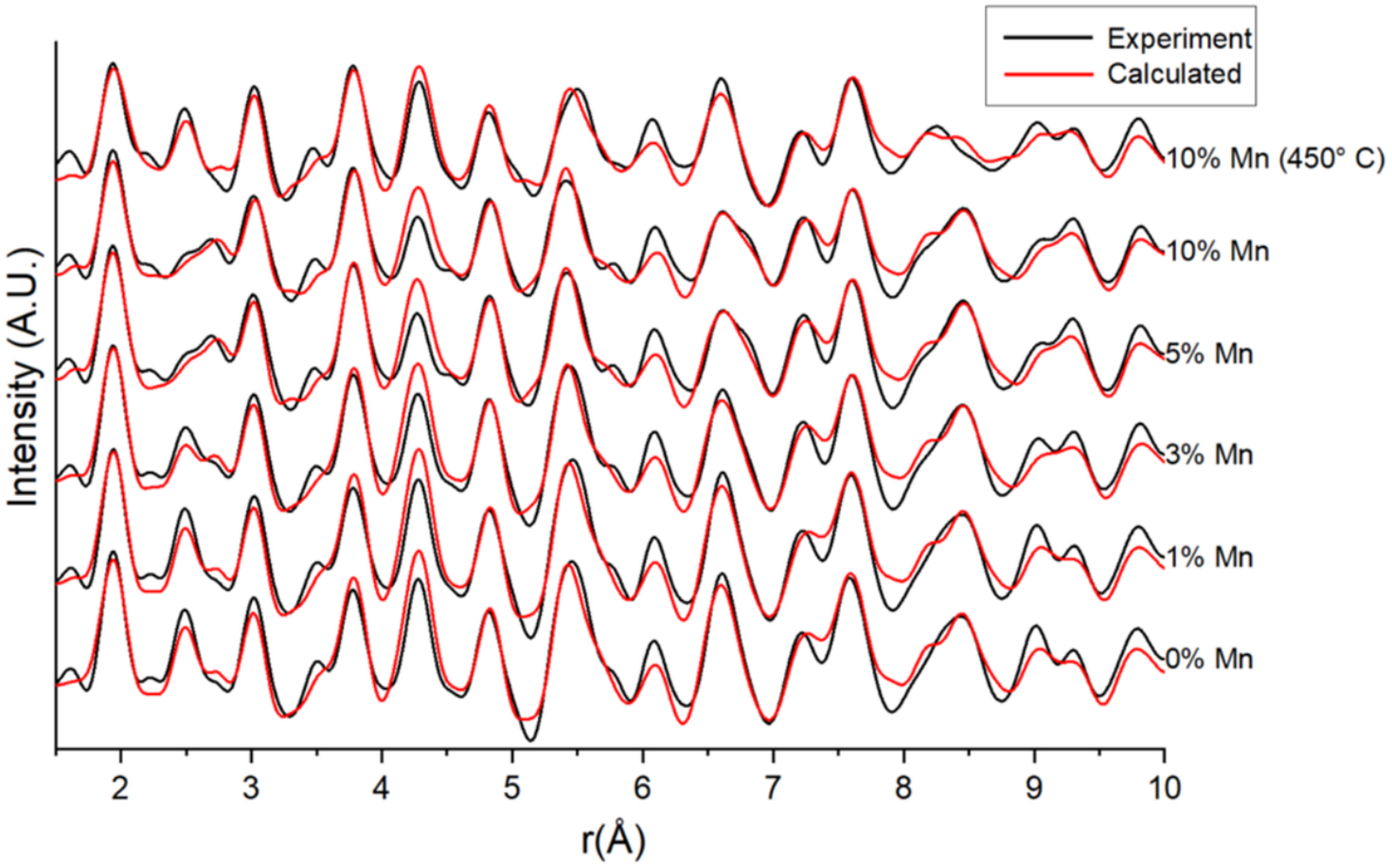

Figure 7

Mean refinements of the PDF data where differences. The formation of carbides from 3-10 % Mn results in the distortion of the FCC/HCP Co-Co peak at 2-3 Å.

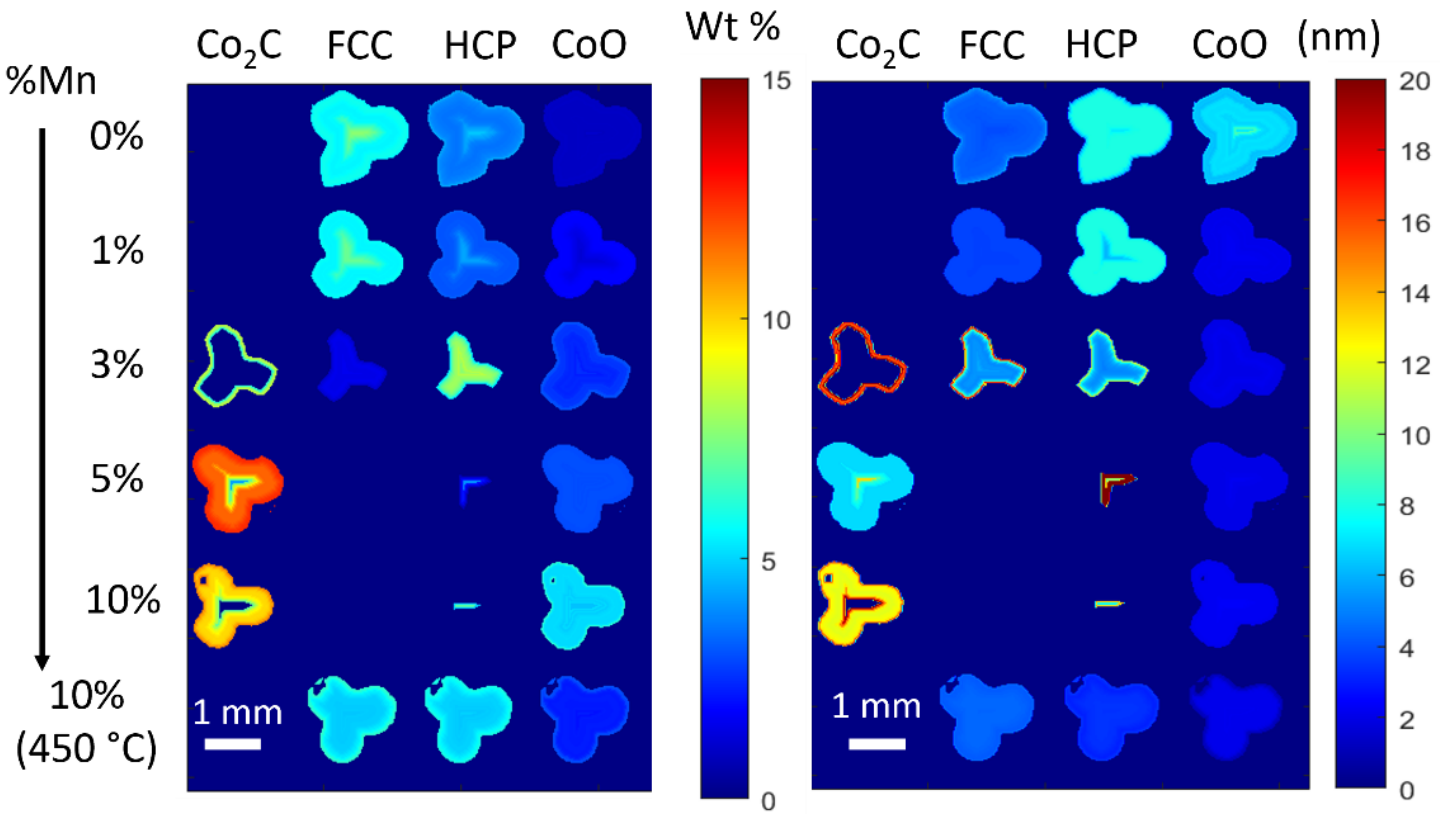

Figure 8

Reconstructed PDF-CT 2D images of the catalytic pellets illustrating the refined wt. % percentage (left) and crystallite size (right) of the different phases present in each pixel of the catalyst pellet for the different Mn loadings. Small CoO particles were present at higher Mn loadings whilst more HCP Co was present at the centre of the 3 % Mn sample.

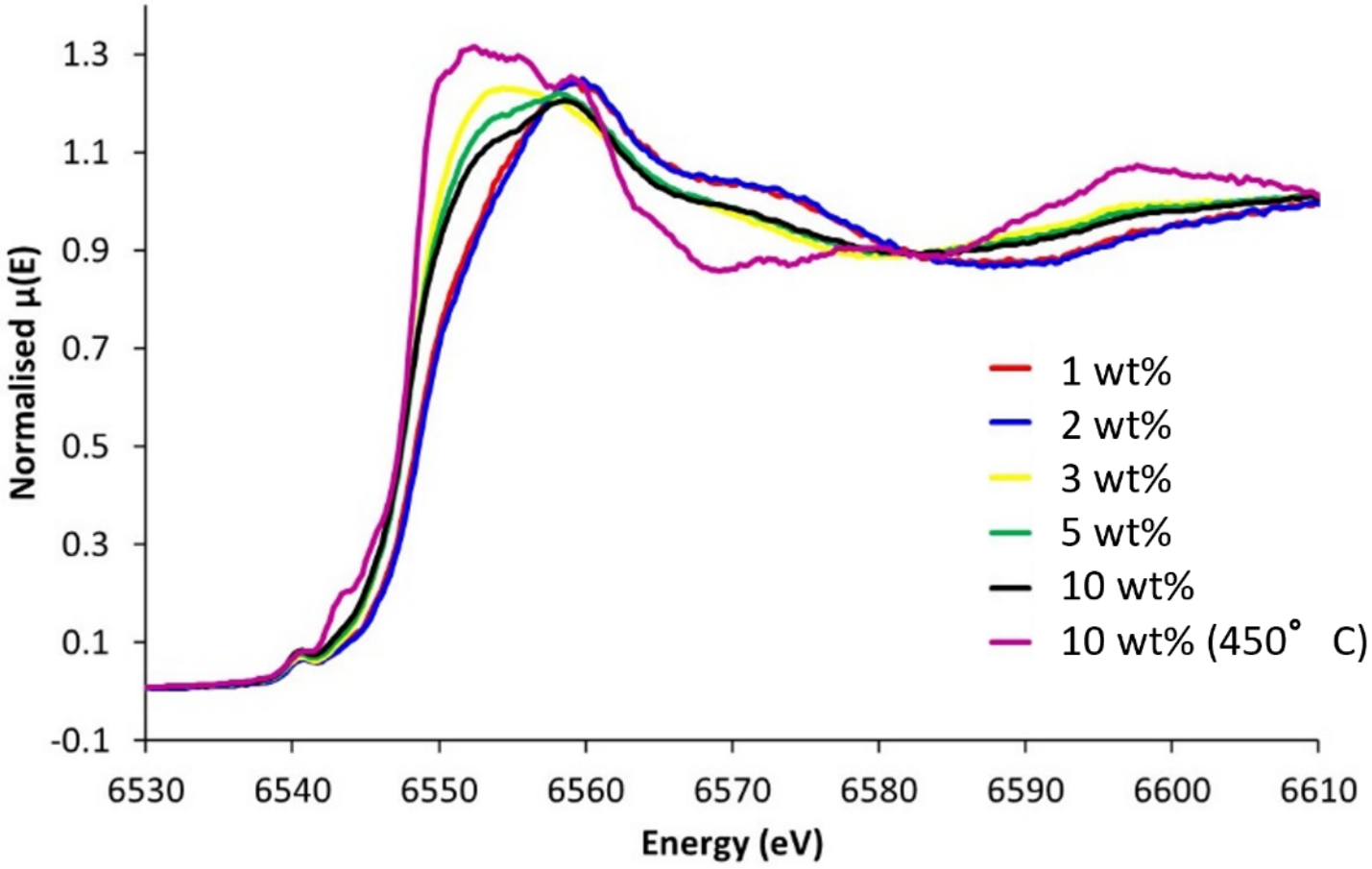

Figure 9

Mn K-edge XANES spectra of $CoMn/TiO_2$ species, as a function of Mn weight loading.

Supplementary Files

This is a list of supplementary files associated with this preprint. Click to download.

- Co2CMnFTSASupp.docx